THE SIZES OF MASSIVE QUIESCENT AND STAR-FORMING GALAXIES AT $z \sim 4$ WITH ZFOURGE AND CANDELS*

Caroline M. S. Straatman[1], Ivo Labbé[1], Lee R. Spitler[2,3], Karl Glazebrook[4], Adam Tomczak[5], Rebecca Allen[4], Gabriel B. Brammer[6], Michael Cowley[2,3], Pieter van Dokkum[7], Glenn G. Kacprzak[4], Lalit Kawinwanichakij[5], Nicola Mehrtens[5], Themiya Nanayakkara[4], Casey Papovich[5], S. Eric Persson[8], Ryan F. Quadri[5], Glen Rees[3], Vithal Tilvi[5], Kim-Vy H. Tran[5], and Katherine E. Whitaker[9]

[1] Leiden Observatory, Leiden University, P.O. Box 9513, 2300 RA Leiden, The Netherlands; straatman@strw.leidenuniv.nl
[2] Australian Astronomical Observatory, P.O. Box 915, North Ryde, NSW 1670, Australia
[3] Department of Physics & Astronomy, Macquarie University, Sydney, NSW 2109, Australia
[4] Centre for Astrophysics and Supercomputing, Swinburne University, Hawthorn, VIC 3122, Australia
[5] George P. and Cynthia W. Mitchell Institute for Fundamental Physics and Astronomy, Department of Physics and Astronomy, Texas A&M University, College Station, TX 77843, USA
[6] Space Telescope Science Institute, 3700 San Martin Drive, Baltimore, MD 21218, USA
[7] Department of Astronomy, Yale University, New Haven, CT 06520, USA
[8] Carnegie Observatories, Pasadena, CA 91101, USA
[9] Astrophysics Science Division, Goddard Space Flight Center, Code 665, Greenbelt, MD 20771, USA

ABSTRACT

We study the rest-frame ultraviolet (UV) sizes of massive ($\sim 0.8 \times 10^{11} M_\odot$) galaxies at $3.4 \leqslant z < 4.2$, selected from the FourStar Galaxy Evolution Survey, by fitting single Sérsic profiles to *Hubble Space Telescope*/WFC3/ F160W images from the Cosmic Assembly Near-infrared Deep Extragalactic Legacy Survey. Massive quiescent galaxies are very compact, with a median circularized half-light radius $r_e = 0.63 \pm 0.18$ kpc. Removing 5/16 (31%) sources with signs of active galactic nucleus activity does not change the result. Star-forming galaxies have $r_e = 2.0 \pm 0.60$ kpc, $3.2 \pm 1.3\times$ larger than quiescent galaxies. Quiescent galaxies at $z \sim 4$ are on average $6.0 \pm 1.7\times$ smaller than at $z \sim 0$ and $1.9 \pm 0.7\times$ smaller than at $z \sim 2$. Star-forming galaxies of the same stellar mass are $2.4 \pm 0.7\times$ smaller than at $z \sim 0$. Overall, the size evolution at $0 < z < 4$ is well described by a power law, with $r_e = 5.08 \pm 0.28(1 + z)^{-1.44 \pm 0.08}$ kpc for quiescent galaxies and $r_e = 6.02 \pm 0.28(1 + z)^{-0.72 \pm 0.05}$ kpc for star-forming galaxies. Compact star-forming galaxies are rare in our sample: we find only 1/14 (7%) with $r_e/(M/10^{11} M_\odot)^{0.75} < 1.5$, whereas 13/16 (81%) of the quiescent galaxies are compact. The number density of compact quiescent galaxies at $z \sim 4$ is $1.8 \pm 0.8 \times 10^{-5}$ Mpc^{-3} and increases rapidly, by $>5\times$, between $2 < z < 4$. The paucity of compact star-forming galaxies at $z \sim 4$ and their large rest-frame UV median sizes suggest that the formation phase of compact cores is very short and/or highly dust obscured.

Key words: cosmology: observations – galaxies: evolution – galaxies: formation – galaxies: high-redshift – infrared: galaxies

1. INTRODUCTION

In recent years, massive quiescent galaxies have been found beyond $z = 3$ (e.g., Chen & Marzke 2004; Wiklind et al. 2008; Fontana et al. 2009; Mancini et al. 2009; Marchesini et al. 2010; Guo et al. 2013; Muzzin et al. 2013; Stefanon et al. 2013; Spitler et al. 2014) and even at $z \sim 4$, when the universe was only 1.5 Gyr old (Straatman et al. 2014). Quiescent galaxies at high redshift ($z > 1$) exhibit compact morphologies, with small effective radii (e.g., Daddi et al. 2005; van Dokkum et al. 2008; Damjanov et al. 2009), which tend to become smaller with increasing redshift (van der Wel et al. 2014). At $z \sim 3$, they have sizes of ~1 kpc, (3–4) × smaller than early-type galaxies of similar stellar mass at $z \sim 0$ (Shen et al. 2003; Mosleh et al. 2013) and (2–3) × smaller than star-forming galaxies at the same redshift.

How compact quiescent galaxies are formed is still unclear. Simulations propose mechanisms in which gas-rich major mergers can induce central starbursts, resulting in a compact merger remnant (Hopkins et al. 2009; Wellons et al. 2015), or in which massive star-forming clumps move to the centers if galaxy disks are unstable (Dekel et al. 2009; Dekel & Burkert 2014). Alternatively, they may have formed in a more protracted process at high redshift, when the universe was more dense (Mo et al. 1998).

To understand these scenarios, it is necessary to identify compact quiescent galaxies and their progenitors at the highest redshifts. Compact star-forming galaxies been found in small numbers at $z = 2$–3 (Barro et al. 2014a, 2014b; Nelson et al. 2014), but many host active galactic nuclei (AGNs), complicating the interpretation of the observations. At the same time, rest-frame ultraviolet (UV) or optically measured sizes of star-forming galaxies may be affected by dust-obscured central regions, thereby increasing their effective radii.

In this work, we investigate the sizes of a stellar-mass complete sample of star-forming and quiescent galaxies at $z \sim 4$. Throughout, we assume a standard ΛCDM cosmology with $\Omega_M = 0.3$, $\Omega_\Lambda = 0.7$ and $H_0 = 70$ km s^{-1} Mpc^{-1}. The adopted photometric system is AB.

2. SAMPLE SELECTION

The galaxies were selected using deep K_s-band images from the FourStar Galaxy Evolution Survey (ZFOURGE; I. Labbé

et al. 2015, in preparation), a near-IR survey with the FourStar Infrared Camera (Persson et al. 2013), covering three $11' \times 11'$ pointings, located in the fields CDFS (Giacconi et al. 2002), COSMOS (Scoville et al. 2007), and UDS (Lawrence et al. 2007). The ZFOURGE K_s-band selected catalogs are at least 80% complete down to $K_s = 24.53$, 24.74 and 25.07 mag in each field, respectively (Papovich et al. 2015). Photometric redshifts and stellar masses were derived using five near-IR medium-bandwidth filters on FourStar (J_1, J_2, J_3, H_s, H_l), which provide a fine sampling of the age-sensitive Balmer/4000 Å break at $1.5 < z < 4$, in combination with public data over a wavelength range $0.3-8\ \mu$m (Straatman et al. 2014). Here, we make additional use of *Hubble Space Telescope* (*HST*)/WFC3/F160W data from CANDELS (Grogin et al. 2011; Koekemoer et al. 2011; Skelton et al. 2014) to examine galaxy sizes and *Spitzer*/MIPS 24 μm data from GOODS-South (PI: Dickinson), COSMOS (PI: Scoville), and SPUDS (PI: Dunlop) to measure infrared flux.

The galaxies in this work have photometric redshifts $3.4 \leqslant z < 4.2$, stellar masses of $\log_{10}(M/M_\odot) \geqslant 10.55$, and K_s-band signal-to-noise ratios (S/Ns) of S/N > 7. They are separated into quiescent and star-forming galaxies according to their rest-frame $U - V$ versus $V - J$ colors (Labbé et al. 2005; Williams et al. 2009; Spitler et al. 2014), yielding 19 quiescent and 25 star-forming galaxies (Straatman et al. 2014). Of these, 34 have *HST*/WFC3/F160W coverage. One quiescent galaxy has an S/N < 3 in F160W and is not included. Another star-forming galaxy with a highly uncertain redshift solution was also rejected from the sample, along with two star-forming galaxies that appear to consist of two sources each in the higher-resolution *HST* images. In total, we study 16 quiescent and 14 star-forming galaxies. We include a control sample at $2 \leqslant z < 3.4$ (326 sources) at similar mass and S/N.

3. GALAXY SIZES FROM *HST*/WFC3 IMAGING

3.1. Sérsic Fits

Sizes and structural parameters were measured by fitting Sérsic (Sérsic 1968) profiles on $6'' \times 6''$ *HST*/WFC3/F160W image stamps using GALFIT (Peng et al. 2010). In particular, we measure the half-light radius, encapsulating half the sources' integrated light. The corresponding parameter in GALFIT is the half-light radius along the semimajor axis ($r_{1/2,\mathrm{maj}}$), which can be converted to circularized effective radius ($r_e = r_{1/2,\mathrm{maj}}\sqrt{(b/a)}$), with b/a as the axis ratio.

We manually subtracted the background in each image stamp, masking sources and using the mode of the pixel flux distribution. Sky estimation in GALFIT was turned off. Neighboring objects at $r > 1\farcs1$ from the source were effectively masked by setting their corresponding pixels in the image to zero flux and increasing those in the noise image by $\times 10^6$. Close neighboring objects were fitted simultaneously.

We created mean point-spread functions (PSFs) for each field by stacking image stamps of bright stars (masking all neighboring sources). As many of the galaxies are small, we investigate the impact of the PSF choice. We repeated the fitting using the hybrid PSF models of van der Wel et al. (2012) and find marginally larger ($<5\%$) sizes. In particular, for the smallest galaxies ($r_e < 0\farcs20$), we find a median $r_e/r_{e,\mathrm{PSF}vdW} = 0.93 \pm 0.05$.

Errors on the individual measurements were calculated using a Monte Carlo procedure. After subtracting the best-fit GALFIT models from the sources, we shifted the residuals by a random number of pixels, added back the model, and used this as input for GALFIT. Repeating this $>200\times$ for each galaxy, errors were calculated as the 1σ variation on these measurements. We report our results in Table 1.

In the fits, the Sérsic index ($n_\mathrm{Sérsic}$) was restricted to $0.1 < n_\mathrm{Sérsic} < 8.0$. If $n_\mathrm{Sérsic}$ reached the extreme value 0.1 or 8.0, GALFIT was rerun while forcing $n_\mathrm{Sérsic} = 1$ for star-forming and $n_\mathrm{Sérsic} = 4$ for quiescent galaxies. These values correspond to the median $n_\mathrm{Sérsic}$ of galaxies with well-constrained fits and $\mathrm{S/N}_\mathrm{F160W} > 15$.

At $z \sim 4$, this happens for 6/16 (38%) quiescent and 2/14 (14%) star-forming galaxies. To explore systematic effects introduced by the choice of profile, we set $n_\mathrm{Sérsic} = 1.0$ or $n_\mathrm{Sérsic} = 4.0$ for bright ($\mathrm{mag}_\mathrm{F160W}(AB) < 24.5$) and compact sources ($r_e < 0\farcs20$) and find on average $r_{e,n=1}/r_{e,n=4} = 0.80 \pm 0.13$, corresponding to a systematic uncertainty of 20%. We add this in quadrature to the uncertainties from the Monte Carlo procedure for each galaxy. Systematic biases of this level do not affect the main results. For comparison, van der Wel et al. (2012) derived typical systematic uncertainties on the size of $\sim 12\%$ for faint F160W $= 24$–26 and small $r_e < 0\farcs3$ galaxies.

As many galaxies have a modest S/N, we tested the reliability of our measurements by a simulation, in which we inserted source models, convolved with the instrument PSF, in the F160W images. These have adopted magnitudes of $25 < \mathrm{mag}_\mathrm{F160W}(AB) < 26$ and a size of $0.06 < r_e('') < 0.3$. We find $r_{e,\mathrm{out}}/r_{e,\mathrm{in}} = 0.97 \pm 0.05$, with $r_{e,\mathrm{in}}$ and $r_{e,\mathrm{out}}$ the input and output effective radii, respectively, showing that we can recover the sizes of faint compact sources without bias. As an additional test, we determine the size distribution of point sources by inserting PSFs in the images and measuring their size. We can constrain the size of bright objects to $0\farcs01$ at 95% confidence, which we adopt as a minimum uncertainty on the sizes.

We crossmatched our sample at $2 \leqslant z < 4.2$ with the size catalogs of van der Wel et al. 2014, based on the 3D-HST photometric catalogs (Skelton et al. 2014). We find that the sizes and Sérsic indices agree well, with a median $r_{e,\mathrm{ZFOURGE}}/r_{e,\mathrm{3DHST}} = 1.004 \pm 0.01$ and $n_\mathrm{ZFOURGE} - n_\mathrm{3DHST} = -0.012 \pm 0.058$.

We test for color gradients between rest-frame UV sizes and rest-frame optical sizes, using a rest-frame color and stellar-mass matched control sample at $z \sim 3$. We find F160W (rest-frame 4000 Å) sizes are $0\% \pm 6\%$ and $6\% \pm 11\%$ smaller than F125W (rest-frame 3000 Å) sizes for star-forming and quiescent galaxies, respectively.

3.2. Stacking

We also measure the average sizes by stacking the background-subtracted image stamps of the two subsamples, normalizing each by mean stellar mass. Neighboring sources were masked. The final stacks were obtained by calculating the mean value at each pixel location of the image stamps.

We ran GALFIT using the same input parameters as for the individual galaxies. Errors were estimated by bootstrapping, i.e., randomly selecting galaxies, recreating the image stacks, and rerunning GALFIT.

Table 1
Properties of 16 Quiescent and 14 Star-forming Galaxies

ID	R.A. (deg)	Decl. (deg)	z	$K_{s,tot}$ (mag)	H_{tot}[a] (mag)	H_{Galfit}[b] (mag)	S/N$_{F160W}$[a]	$M/10^{11}$ ($M_\odot$)	r_{KRON}[a] (′)	$r_{1/2,maj}$ (′)	r_e (kpc)	b/a	$n_{sércic}$	A_v	24 μm[c,d] (μJy)
QUIESCENT															
ZF-CDFS-209	53.1132774	−27.8698730	3.56	22.6	24.1	24.3 ± 0.0	64.6	0.76	0.23	0.06 ± 0.01	0.27 ± 0.07	0.37 ± 0.08	4.00	0.3	−0.9 ± 3.5
ZF-CDFS-403	53.0784111	−27.8598385	3.660[e]	22.4	23.7	23.5 ± 0.0	118.0	1.15	0.22	0.12 ± 0.03	0.82 ± 0.18	0.85 ± 0.05	7.78 ± 0.94	0.8	99.8 ± 148.5[c]
ZF-CDFS-4719	53.1969414	−27.7604313	3.59	23.4	25.2	25.2 ± 0.1	33.5	0.45	0.23	0.12 ± 0.03	0.60 ± 0.14	0.48 ± 0.08	1.88 ± 0.84	0.3	1.9 ± 3.4
ZF-CDFS-4907	53.1812820	−27.7564163	3.46	23.6	25.0	25.1 ± 0.1	38.2	0.40	0.28	0.08 ± 0.02	0.56 ± 0.13	0.86 ± 0.12	3.28 ± 0.90	0.8	1.4 ± 3.6
ZF-CDFS-5657	53.0106506	−27.7416019	3.56	23.0	24.6	24.2 ± 0.1	26.7	0.76	0.33	0.52 ± 0.16	3.22 ± 0.93	0.72 ± 0.11	4.45 ± 0.98	0.3	1.7 ± 3.8[c]
ZF-CDFS-617	53.1243553	−27.8516121	3.700[e]	22.3	23.5	23.5 ± 0.0	135.1	0.69	0.22	0.10 ± 0.02	0.55 ± 0.11	0.59 ± 0.03	4.00	0.3	86.3 ± 3.4[c,d]
ZF-COSMOS-13129	150.1125641	2.3765368	3.81	23.6	25.2	24.9 ± 0.1	10.8	1.78	0.46	0.52 ± 0.13	2.15 ± 0.48	0.34 ± 0.08	0.56 ± 0.24	0.6	110.1 ± 10.2[d]
ZF-COSMOS-13172	150.0615082	2.3786869	3.55	22.4	24.4	24.4 ± 0.1	37.2	1.45	0.27	0.08 ± 0.02	0.49 ± 0.12	0.64 ± 0.13	3.94 ± 1.11	0.6	2.7 ± 7.6
ZF-COSMOS-13414	150.0667114	2.3823516	3.57	23.4	25.4	25.4 ± 0.1	14.0	0.44	0.32	0.20 ± 0.06	0.83 ± 0.29	0.34 ± 0.14	1.51 ± 1.00	0.2	7.1 ± 8.7
ZF-UDS-10684	34.3650742	−5.1488328	3.95	24.1	25.9	25.2 ± 0.2	8.5	0.85	0.32	0.50 ± 0.17	2.42 ± 0.77	0.47 ± 0.18	4.63 ± 1.68	1.0	8.8 ± 12.8
ZF-UDS-11483	34.3996315	−5.1363320	3.63	23.6	26.0	25.9 ± 0.2	8.9	1.02	0.35	0.11 ± 0.05	0.52 ± 0.25	0.43 ± 0.24	4.59 ± 2.01	1.0	1.8 ± 10.2
ZF-UDS-2622	34.2894516	−5.2698011	3.77	23.0	24.6	24.5 ± 0.1	29.9	0.87	0.30	0.13 ± 0.03	0.76 ± 0.19	0.66 ± 0.10	4.00	0.9	12.2 ± 10.6
ZF-UDS-3112	34.2904282	−5.2620673	3.53	23.2	24.9	24.9 ± 0.1	25.7	0.43	0.30	0.07 ± 0.02	0.39 ± 0.13	0.66 ± 0.19	4.00	0.0	−10.9 ± 10.6
ZF-UDS-5418	34.2937546	−5.2269468	3.53	23.3	24.9	24.9 ± 0.1	20.7	0.44	0.30	0.07 ± 0.02	0.50 ± 0.14	0.83 ± 0.17	4.00	0.5	48.4 ± 10.6
ZF-UDS-6119	34.2805405	−5.2171388	4.05	23.8	25.5	25.4 ± 0.2	10.6	0.55	0.32	0.26 ± 0.15	1.26 ± 0.75	0.49 ± 0.20	4.00	1.0	−12.5 ± 8.7
ZF-UDS-9526	34.3381844	−5.1661916	3.97	24.2	25.9	25.8 ± 0.3	11.5	0.89	0.21	0.10 ± 0.05	0.39 ± 0.35	0.34 ± 0.24	2.03 ± 2.28	1.8	38.7 ± 8.7[c,d]
STACK	⋯	⋯	3.66	⋯	⋯	⋯	⋯	0.81	⋯	⋯	0.85 ± 0.35	⋯	4.14 ± 0.71	⋯	⋯
STAR-FORMING															
ZF-CDFS-261	53.0826530	−27.8664989	3.40	23.2	24.2	24.5 ± 0.1	27.1	1.07	0.40	0.61 ± 0.14	3.54 ± 0.80	0.62 ± 0.06	1.21 ± 0.25	1.9	12.1 ± 4.4[c]
ZF-CDFS-400	53.1025696	−27.8606110	4.10	24.3	25.1	25.1 ± 0.2	23.9	0.52	0.33	0.24 ± 0.13	1.45 ± 0.78	0.78 ± 0.11	3.40 ± 1.40	0.9	31.3 ± 3.6[c,d]
ZF-CDFS-509	53.1167717	−27.8559704	3.95	24.2	25.1	25.0 ± 0.0	29.1	0.41	0.25	0.31 ± 0.06	1.55 ± 0.32	0.52 ± 0.05	0.51 ± 0.17	1.0	−4.5 ± 4.1
ZF-COSMOS-12141	150.0815277	2.3637166	4.00	24.0	24.7	24.1 ± 0.2	18.8	0.45	0.34	0.81 ± 0.27	3.58 ± 1.09	0.40 ± 0.10	4.92 ± 1.35	1.1	0.9 ± 8.0
ZF-COSMOS-3784	150.1817627	2.2390490	3.58	22.9	23.9	23.8 ± 0.1	26.6	0.36	0.38	0.53 ± 0.13	3.40 ± 0.78	0.77 ± 0.10	1.88 ± 0.33	0.5	−2.4 ± 10.2
ZF-UDS-11279	34.3843269	−5.1402941	3.72	25.0	26.6	26.4 ± 0.3	4.5	0.46	0.32	0.15 ± 0.10	0.96 ± 0.54	0.81 ± 0.23	1.00	2.2	29.3 ± 12.5
ZF-UDS-4432	34.3581772	−5.2409291	3.76	23.8	24.5	24.2 ± 0.2	17.5	0.83	0.37	0.75 ± 0.39	3.61 ± 1.74	0.46 ± 0.11	4.27 ± 1.65	1.5	669.0 ± 10.7[d]
ZF-UDS-4449	34.3409157	−5.2405076	3.84	23.1	24.4	24.9 ± 0.1	17.2	0.41	0.35	0.44 ± 0.10	1.90 ± 0.41	0.38 ± 0.07	0.23 ± 0.14	1.0	⋯
ZF-UDS-4462	34.3408661	−5.2402906	3.92	23.0	24.0	24.0 ± 0.1	27.9	0.39	0.26	0.39 ± 0.09	2.09 ± 0.45	0.60 ± 0.08	1.69 ± 0.27	0.8	22.6 ± 9.4
ZF-UDS-5617	34.3407745	−5.2240300	4.17	24.5	26.0	24.5 ± 0.3	6.3	0.42	0.37	2.33 ± 0.72	10.74 ± 3.30	0.45 ± 0.18	4.92 ± 1.51	1.3	9.5 ± 9.7
ZF-UDS-8379	34.4104004	−5.1821156	3.77	23.8	25.2	25.2 ± 0.1	14.0	0.65	0.25	0.30 ± 0.07	1.50 ± 0.34	0.50 ± 0.09	0.52 ± 0.28	2.6	355.8 ± 25.0[d]
ZF-UDS-8399	34.4105759	−5.1825032	3.44	24.4	25.3	25.0 ± 0.1	11.9	0.43	0.23	0.69 ± 0.16	2.28 ± 0.49	0.20 ± 0.05	0.14 ± 0.17	2.5	106.6 ± 25.1[d]
ZF-UDS-8580	34.3544159	−5.1797152	4.07	23.7	24.6	24.7 ± 0.1	19.8	0.66	0.26	0.36 ± 0.08	1.82 ± 0.37	0.54 ± 0.05	0.18 ± 0.09	1.1	7.1 ± 8.4
ZF-UDS-9165	34.3225441	−5.1713767	4.06	23.4	24.2	24.6 ± 0.1	33.8	0.68	0.31	0.11 ± 0.03	0.66 ± 0.14	0.72 ± 0.09	1.00	0.3	43.3 ± 10.1[d]
STACK	⋯	⋯	3.84	⋯	⋯	⋯	⋯	0.55	⋯	⋯	2.62 ± 1.15	⋯	2.17 ± 2.41	⋯	⋯

Notes.
[a] F160W, S/N, and circularized KRON radius (r_{KRON}) crossmatched from 3D-HST (Skelton et al. 2014; van der Wel et al. 2014).
[b] GALFIT and 3D *HST* magnitudes are consistent within 0.05 ± 0.03 mag on average, with a dispersion of 0.24.
[c] X-ray detection (Xue et al. 2011).
[d] $L_{IR} > 7 \times 10^{12} L_\odot$.
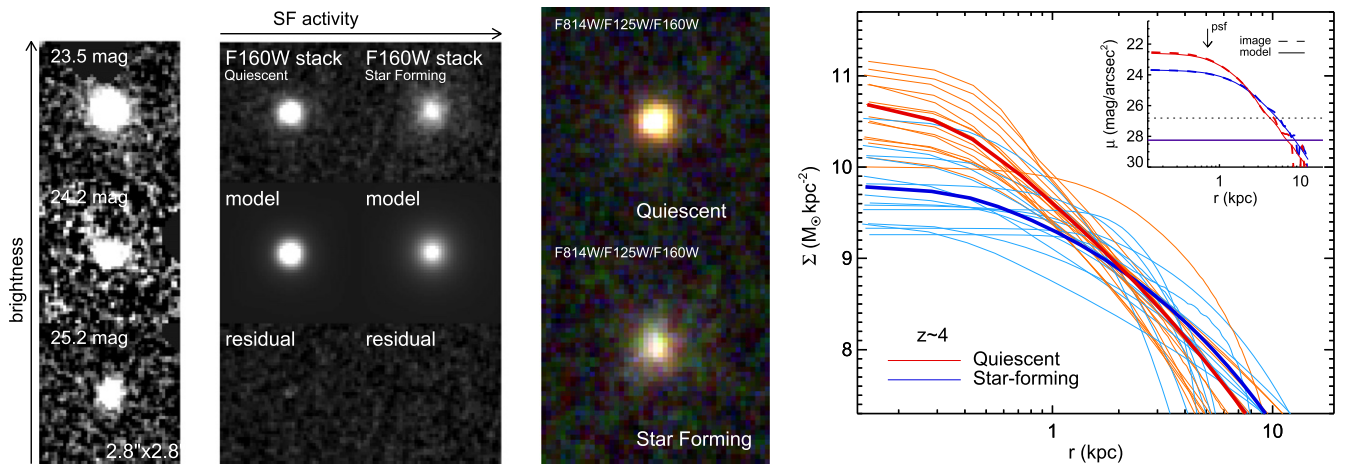[e] *zspec* (Szokoly et al. 2004).

Figure 1. Left: example galaxies at $z \sim 4$ of varying magnitude. Second: stacks of the quiescent and star-forming subsamples, with the corresponding best-fit models and residuals after subtracting the models. Third: F814W/F125W/F160W stack color composites. Right: stellar-mass surface density profiles. Thin orange and blue lines represent individual measurements of quiescent and star-forming galaxies, respectively. Thick lines represent the stacks. The inset shows the surface brightness profiles of the stacks, with horizontal lines indicating 3σ brightness limits of 28.3 mag arcsec^{-2}, measured in annuli of 0″06 (0.43 kpc) width at $r > 1''$. The background limit for individual galaxies (dotted line) is 26.8 mag arcsec^{-2}.

In Figure 1, we show the stacks and examples of individual galaxies. The stack of quiescent galaxies is redder than the stack of star-forming galaxies and has a more compact morphology. We also show stellar-mass surface density profiles ($\Sigma(M_\odot/\mathrm{kpc}^2) = M(<r)/(\pi r^2)$), obtained from the light profile measured in concentric apertures of radius r and assuming a constant mass-to-light ratio. For the stacked profiles, we used the mean mass of the galaxies in each stack. They are consistent with the individual profiles within the uncertainties, suggesting that the stack does not reveal an extended low surface brightness component, down to a surface brightness limit of 28.3 mag arcsec^{-2}.

3.3. Contamination by AGN

A substantial fraction of sources show signs of AGN activity either from X-ray detections or strong 24 μm (rest-frame 5 μm, tracing hot dust). As WFC3/F160W ($\lambda = 1.5396 \mu$m) corresponds to rest-frame 2960–3500 Å (UV) at $3.4 \leqslant z < 4.2$, it could be that an AGN is dominating their central light, leading to small sizes of the single Sérsic fits.

In the quiescent sample, we find four X-ray-detected galaxies, two of which are spectroscopically confirmed type-II QSOs (Szokoly et al. 2004). Another has strong 24 μm, which could either point toward dust-obscured star formation or AGN activity. Several have small positive residuals after subtracting the best fit, suggesting the presence of a central point source. These 5/16 (31%) galaxies were re-fit with two components, a Sérsic model, and a point-source-like model (represented by a Gaussian with FWHM = 0.1 pixels) to trace possible AGN light. In these models, the point source accounts for 4.3%–68% of the total light (with 57% and 68% for the type-II QSOs, but on average 6.2% for the remaining three AGN candidates). The average size of the Sérsic component increases by 1.5× (from a median $r_e = 0.13 \pm 0''12$ to $r_e = 0.20 \pm 0''03$).

Among the star-forming galaxies two are X-ray detected and four are very bright at 24 μm ($L > 7 \times 10^{12} L_\odot$ or SFR $> 1200 M_\odot$ yr^{-1}). Re-fitting with a two-component model

attributes 0.9%–39.4% of the light to a point source, while the extended component changes in size by 0.65× (from $r_e = 0.31 \pm 0''15$ to $r_e = 0.19 \pm 0''02$). We note that for the most extended sources, adding central light reduces the Sérsic index $n_{\mathrm{Sérsic}}$ of the extended component and can result in a smaller r_e.

We additionally estimated the possible AGN contribution from the galaxy spectral energy distributions (SEDs). We first determine the best-fitting power law blueward of rest-frame 0.35 μm and at observed 8 μm (Kriek et al. 2009). Then we fit the sum of the power law and the original best-fit EAZY template (Brammer et al. 2008) to the data. The contribution of the AGN power-law template to F160W is 1.1%–7.4% for the five quiescent galaxies and 0.9%–2.9% for the six star-forming galaxies.

While the two-component fits and SEDs indicate that a point-source contribution is probably small, the true contribution and its effect on the sizes remain unclear.

4. RESULTS

We show the effective radius as a function of stellar mass in Figure 2. Quiescent galaxies at $z \sim 4$ are very compact, with a bootstrapped median size $r_e = 0.63 \pm 0.18$ kpc. When we remove AGNs, we find a similar result: $r_e = 0.57 \pm 0.18$ kpc.

Star-forming galaxies have $r_e = 2.0 \pm 0.60$ kpc. They are $3.2 \pm 1.3\times$ larger than quiescent galaxies. Both samples have a large spread in size, with some almost as large as at $z \sim 0$, showing that at $z \sim 4$ the population is already very diverse. On average, the sizes lie well below the $z \sim 0$ relation (Mosleh et al. 2013), by $6.0 \pm 1.7\times$ for quiescent and $2.4 \pm 0.7\times$ for star-forming galaxies. Quiescent galaxies are also $1.9 \pm 0.7\times$ smaller than at $2 \leqslant z < 2.2$.

In Figure 3, we show Sérsic index versus size for the $z \sim 4$ galaxies and a sample at a similar mass at $2 \leqslant z < 2.2$. Star-forming galaxies have a smaller Sérsic index, with, on average, $n_{\mathrm{Sérsic}} = 1.3 \pm 0.7$, compared to $n_{\mathrm{Sérsic}} = 3.2 \pm 1.2$ for quiescent galaxies. The difference between the two populations is also clear from the stellar-mass density profiles in Figure 1, with quiescent galaxies having steeper profiles and more centralized
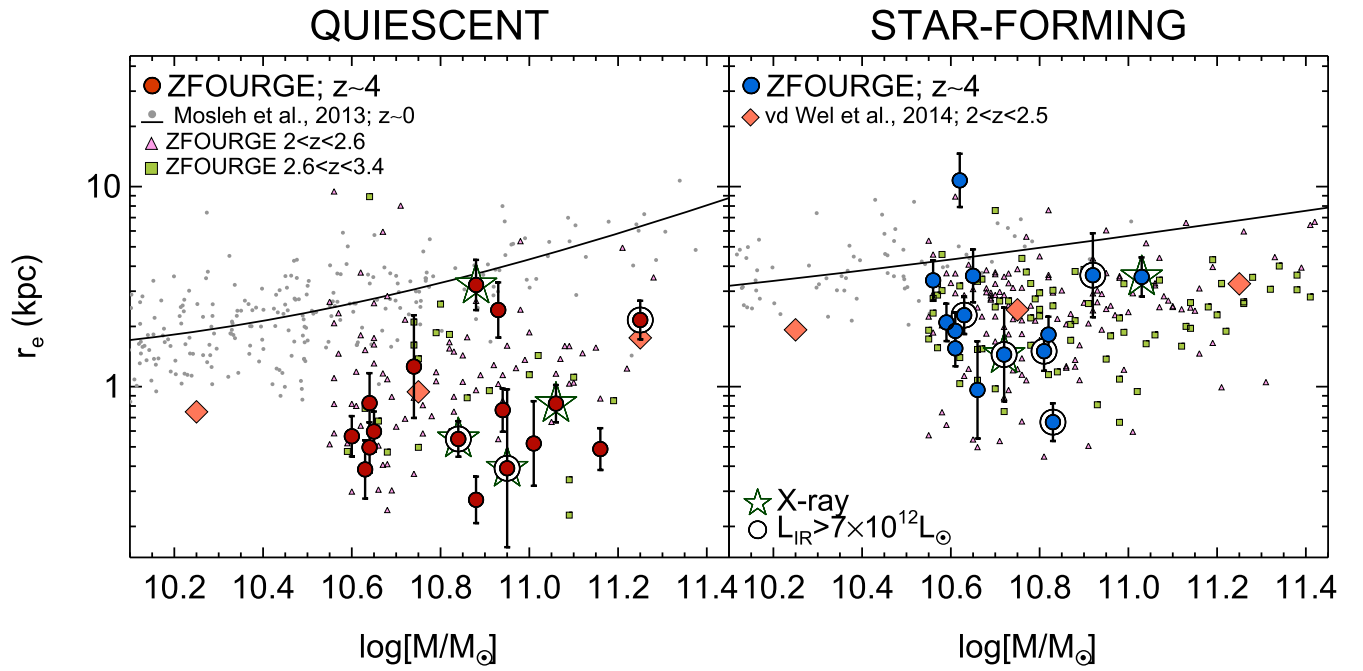
Figure 2. Circularized effective radius for galaxies at $z \sim 4$. In purple and green, we show our control sample at $2 \leqslant z < 2.6$ and $2.6 \leqslant z < 3$ and in orange the median of van der Wel et al. (2014) at $2 < z < 2.5$. The black solid line is the $z \sim 0$ relation of Mosleh et al. (2013). X-ray detections and bright 24 μm sources are indicated with stars and open circles. The median sizes are $r_e = 0.63 \pm 0.18$ kpc (quiescent galaxies) and $r_e = 2.0 \pm 0.60$ kpc (star-forming galaxies).

flux. In Figure 3, we also plot $\langle \Sigma \rangle_{max}$, defined as the average stellar-mass density inside the radius where $\Sigma(M_\odot \, kpc^{-2})$ falls of by a factor of two (Hopkins et al. 2010), with uncertainties from the Monte Carlo procedure described in Section 3.1.

Quiescent galaxies at $z \sim 4$ have a median $\langle \Sigma \rangle_{max} = 3.3 \pm 1.1 \times 10^{10} M_\odot \, kpc^{-2}$, much higher ($\sim 10 \times$) than for star-forming galaxies: $\langle \Sigma \rangle_{max} = 0.3 \pm 0.1 \times 10^{10} M_\odot \, kpc^{-2}$, and more similar to $2 \leqslant z < 2.2$ quiescent galaxies: $\langle \Sigma \rangle_{max} = 1.7 \pm 0.3 \times 10^{10} M_\odot \, kpc^{-2}$.

When stacking, we find $r_e = 0.85 \pm 0.35$ kpc (quiescent) and $r_e = 2.6 \pm 1.2$ kpc (star forming), and Sérsic indices $n_{sérsic} = 4.17 \pm 0.90$ and $n_{sérsic} = 2.18 \pm 2.03$, respectively. The effective radius of the quiescent stack is slightly larger than the median of the individual galaxies, by $1.3 \pm 0.3 \times$ at $< 1\sigma$ significance, but overall the results are consistent.

In Figure 4, we show the median sizes at the respective mean redshifts of the two subsamples. Comparing with lower redshift, they continue to follow a trend of decreasing size with increasing redshift. Our control sample of galaxies at $2 \leqslant z < 3.4$ with $10.5 \leqslant \log_{10}(M/M_\odot) < 11$ corresponds well with the results of van der Wel et al. (2014), which suggest the same trend.

We fit a relation of the form $r_e = A(1+z)^B$ kpc at $0 < z < 4$, using the measurements of van der Wel et al. (2014) at $z < 2$. We find $r_e = 5.08 \pm 0.28(1+z)^{-1.44 \pm 0.08}$ kpc for quiescent and $r_e = 6.02 \pm 0.28(1+z)^{-0.72 \pm 0.05}$ kpc for star-forming galaxies. We note that our sample at $z \sim 4$ includes higher-mass ($\log_{10}(M/M_\odot) \geqslant 11$) galaxies. If we remove the most massive galaxies, we find the same evolutionary relation.

To test for incompleteness for diffuse galaxies, we redshift a stellar-mass matched sample with $r > 2$ kpc and $n_{Sérsic} < 2.5$ at $z \sim 2.5$ to $z = 3.7$ and find 70% completeness.

5. DISCUSSION

Our results show that the galaxies at $z \sim 4$ in this study obey similar relations between size and star-forming activity as galaxies at lower redshift. Quiescent galaxies are compact, while star-forming galaxies are more extended and diffuse. The difference is also clear when selecting purely on size: if we define compactness as $r_e/(M/10^{11}M_\odot)^{0.75} < 1.5$ (van der Wel et al. 2014), 13/14 (93%) of massive compact galaxies would be classified as quiescent, and 13/16 (81%) of larger galaxies as star forming (Figure 3).

The number density of compact, $\log_{10}(M/M_\odot) \geqslant 10.55$, quiescent galaxies at $z \sim 4$ is $1.8 \pm 0.8 \times 10^{-5}$ Mpc^{-3}, increasing by $>5 \times$ between $3.4 \leqslant z < 4.2$ and $2 \leqslant z < 2.2$, toward $1.0 \pm 0.3 \times 10^{-4}$ Mpc^{-3}. This suggests we are probing a key era of their formation, and we would expect to see their star-forming progenitors in abundance.

Small effective radii for star-forming galaxies have been reported at $z = 2$–3 (Barro et al. 2014a, 2014b; Nelson et al. 2014). They are rare in our sample: we find 1/14 with $r_e/(M/10^{11}M_\odot)^{0.75} < 1.5$. On average, star-forming galaxies at $z \sim 4$ are twice as large as quiescent galaxies at $z \sim 2$. If they are the direct progenitors of $z < 4$ compact quiescent galaxies, we expect them to be similar, not only in size, but also in Sérsic index and central surface density (Nelson et al. 2014). However, we find smaller $n_{Sérsic}$ for star-forming galaxies, while the central densities indicate that they must increase in $\langle \Sigma \rangle_{max}$ by 5–$10 \times$ to match the more cuspy profiles of $z = 2$–4 quiescent galaxies.

In a recent simulation, Wellons et al. (2015; Ilustris) trace the evolution of galaxies to $z = 2$. They indeed identified two theoretical formation tracks: one in which a brief and intense central starburst prompted by a gas-rich major merger causes the galaxies' half-mass radius to decrease dramatically. The second is that of a more gradual but early formation, with small
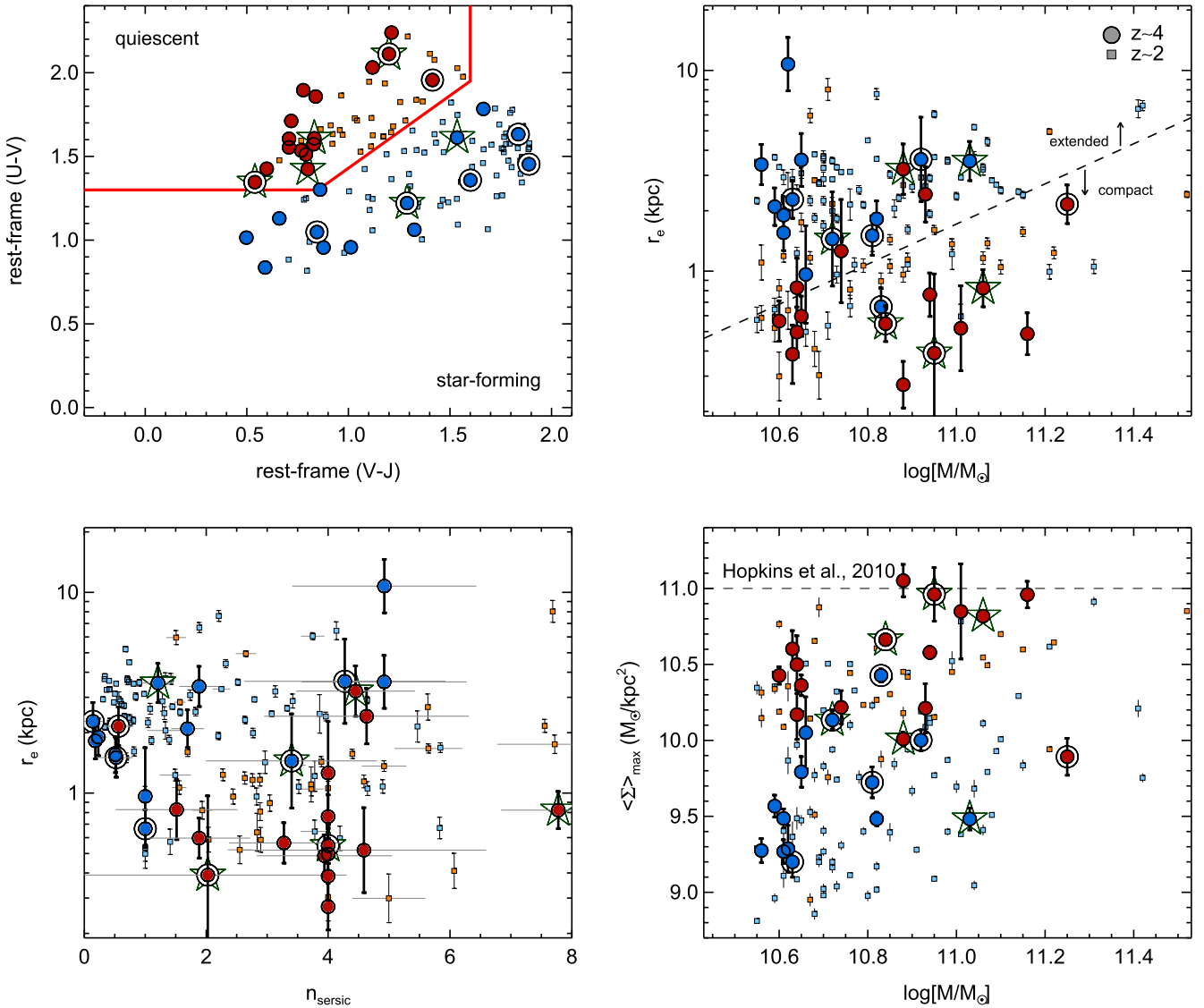
Figure 3. Top left: UVJ diagram of $z \sim 4$ galaxies (symbols as in Figure 2). Small squares represent galaxies at $2.0 \leqslant z < 2.2$. Top right: stellar mass vs. size. Bottom left: Sérsic index vs. size. Bottom right: stellar mass vs. maximum stellar-mass density. The horizontal dashed line is the empirical limit of Hopkins et al. (2010). Only one $z \sim 4$ star-forming galaxy is compact. On average, quiescent galaxies have smaller sizes, higher Sérsic indices, and higher central densities than star-forming galaxies.

galaxy sizes due to the higher density of the universe. In the second case, nearly all of the stellar mass is in place at $z > 4$.

Comparing with the observations, we find that 19/44 of massive $z \sim 4$ galaxies are classified as quiescent, whereas all similarly massive galaxies in Illustris are still actively star forming, with a typical SFR $= 100-200 M_\odot$ yr^{-1}. This level of star formation is ruled out at $>3\sigma$ by *Herschel* observations of the $z \sim 4$ quiescent galaxies (Straatman et al. 2014). At the same time, the fraction of compact galaxies in our sample is 47%, versus $\sim 20\%$ in Illustris. Hence, massive galaxies appear to quench their star formation earlier and to be more compact than in simulations.

The paucity of compact star-forming galaxies at $z \sim 4$ and their large median rest-frame UV size is puzzling. At face value, it suggests that the rapid increase in number density of compact quiescent galaxies cannot be explained by simple shutdown of star formation in typical star-forming galaxies of similar stellar mass. A possible solution is a rapidly forming dense core, i.e., a central starburst. Then the chance to observe the progenitors in our sample is small, as it is proportional to

the duration of the main star-forming episode. For example, if compact cores of $2 \leqslant z < 2.2$ quiescent galaxies formed at random times between $2.5 < z < 6$, with a typical 100 Myr central starburst duration, their predicted number density at $z \sim 4$ would be $\sim 6 \times 10^{-6}$ Mpc^{-3}. The observed number density of compact star-forming galaxies is $1.4 \pm 1.4 \times 10^{-6}$ Mpc^{-3}: smaller, but in a similar range given the large uncertainties.

We note that the remarkably high fraction of quiescent galaxies at $z \sim 4$ (Figure 4) is still uncertain. Current limits on the average dust-obscured SFR are weak ($<75 M_\odot$ yr^{-1}(3σ); Straatman et al. 2014); hence, some of the quiescent galaxies could be star forming. Cosmic variance is significant ($\sim 30\%$). Highly obscured massive star-forming galaxies might also be missed by near-IR surveys (e.g., Daddi et al. 2009; Caputi et al. 2012), although the abundance and redshift distribution of such galaxies is still very uncertain. Finally, extended ($r > 3$ kpc) galaxies with small $n_{\text{Sérsic}}$ and low surface brightness are more difficult to detect than compact galaxies (e.g., Trujillo et al. 2006).
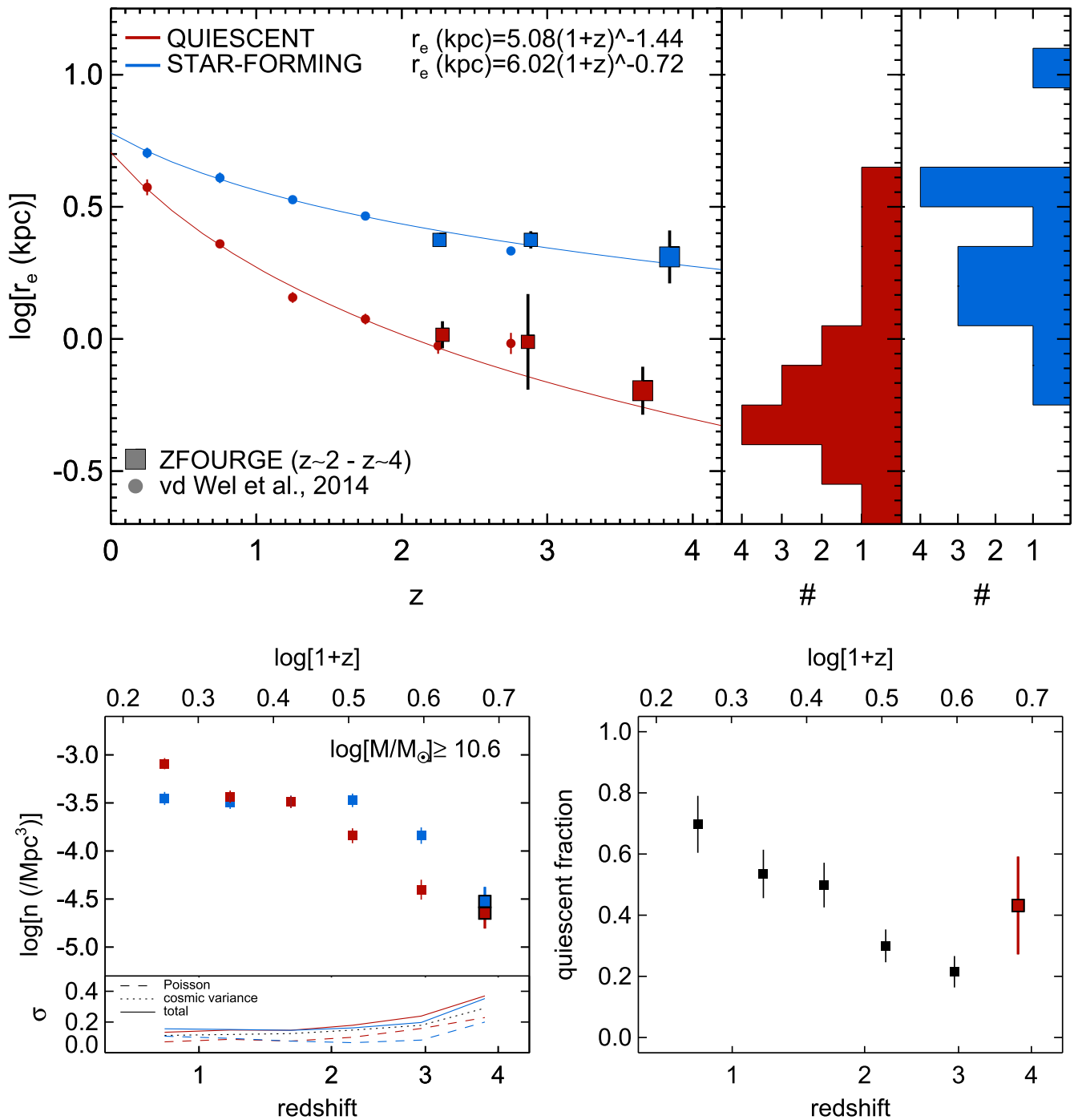
Figure 4. Top: effective radius vs. redshift for galaxies with $10.5 < \log_{10}(M/M_\odot) < 11.0$ at $2 \leqslant z < 3.4$ (van der Wel et al. 2014) and $\log_{10}(M/M_\odot) \geqslant 10.55$ at $3.4 \leqslant z < 4.2$ (filled squares). Quiescent galaxies follow $r_e = 5.08 \pm 0.28(1+z)^{-1.44\pm0.08}$ kpc and star-forming galaxies $r_e = 6.02 \pm 0.28(1+z)^{-0.72\pm0.05}$ kpc (solid curves). The histograms show the size distribution at $z \sim 4$. Bottom: number density (left) and quiescent fraction (right), including galaxies without *HST* coverage. In the left panel, we include the relative Poissonian uncertainties and the effect of cosmic variance. The total uncertainty on number density increases to 40% at $z \sim 4$.

We caution that the light profiles measured here may not be representative of the stellar-mass distribution due to color gradients, with rest-frame UV sizes larger than rest-frame optical sizes. This would imply that the size evolution is stronger. However, using a control sample at $z \sim 3$, we find no difference between UV and optical, consistent with van der Wel et al. (2014), who show this effect is $\lesssim$10% at $z \sim 2$ and decreasing with redshift.

Galaxy sizes may also be overestimated if dust is obscuring a central starburst. Submillimeter sizes of obscured starbursting galaxies could be small: <1 kpc (e.g., Ikarashi et al. 2014; Simpson et al. 2015). A direct comparison of ALMA submillimeter and rest-frame optical/UV morphologies for the same objects with measured stellar mass will reveal the effect of dust obscuration on UV/optically measured galaxy sizes.

REFERENCES

Barro, G., Faber, S. M., Pérez-González, P. G., et al. 2014a, ApJ, 791, 52
Barro, G., Trump, J. R., Koo, D. C., et al. 2014b, ApJ, 795, 145
Brammer, G. B., van Dokkum, P. G., & Coppi, P. 2008, ApJ, 686, 1503
Caputi, K. I., Dunlop, J. S., McLure, R. J., et al. 2012, ApJL, 750, L20
Chen, H.-W., & Marzke, R. O. 2004, ApJ, 615, 603
Daddi, E., Renzini, A., Pirzkal, N., et al. 2005, ApJ, 626, 680
Daddi, E., Dannerbauer, H., Stern, D., et al. 2009, ApJ, 694, 1517
Damjanov, I., McCarthy, P. J., Abraham, R. G., et al. 2009, ApJ, 695, 101
Dekel, A., & Burkert, A. 2014, MNRAS, 438, 1870
Dekel, A., Birnboim, Y., Engel, G., et al. 2009, Nature, 457, 451
Fontana, A., Santini, P., Grazian, A., et al. 2009, A&A, 501, 15
Giacconi, R., Zirm, A., Wang, J., et al. 2002, ApJS, 139, 369
Grogin, N. A., Kocevski, D. D., Faber, S. M., et al. 2011, ApJS, 197, 35
Guo, Y., Ferguson, H. C., Giavalisco, M., et al. 2013, ApJS, 207, 24
Hopkins, P. F., Hernquist, L., Cox, T. J., Keres, D., & Wuyts, S. 2009, ApJ, 691, 1424
Hopkins, P. F., Murray, N., Quataert, E., & Thompson, T. A. 2010, MNRAS, 401, L19
Ikarashi, S., Ivison, R. J., Caputi, K. I., et al. 2014, ApJL, submitted (arXiv: 1411.5038)
Koekemoer, A. M., Faber, S. M., Ferguson, H. C., et al. 2011, ApJS, 197, 36
Kriek, M., van Dokkum, P. G., Labbé, I., et al. 2009, ApJ, 700, 221
Labbé, I., Huang, J., Franx, M., et al. 2005, ApJL, 624, L81
Lawrence, A., Warren, S. J., Almaini, O., et al. 2007, MNRAS, 379, 1599
Mancini, C., Matute, I., Cimatti, A., et al. 2009, A&A, 500, 705
Marchesini, D., Whitaker, K. E., Brammer, G., et al. 2010, ApJ, 725, 1277
Mo, H. J., Mao, S., & White, S. D. M. 1998, MNRAS, 295, 319
Mosleh, M., Williams, R. J., & Franx, M. 2013, ApJ, 777, 117
Muzzin, A., Marchesini, D., Stefanon, M., et al. 2013, ApJ, 777, 18
Nelson, E., van Dokkum, P., Franx, M., et al. 2014, Natur, 513, 394
Papovich, C., Labbé, I., Quadri, R., et al. 2015, ApJ, 803, 26
Peng, C. Y., Ho, L. C., Impey, C. D., & Rix, H.-W. 2010, AJ, 139, 2097
Persson, S. E., Murphy, D. C., Smee, S., et al. 2013, PASP, 125, 654
Scoville, N., Aussel, H., Brusa, M., et al. 2007, ApJS, 172, 1
Sérsic, J. L. 1968, Atlas de Galaxias Australes (Córdoba, Argentina: Observatorio Astronómico)
Shen, S., Mo, H. J., White, S. D. M., et al. 2003, MNRAS, 343, 978
Simpson, J. M., Smail, I., Swinbank, A. M., et al. 2015, ApJ, 799, 81
Skelton, R. E., Whitaker, K. E., Momcheva, I. G., et al. 2014, ApJS, 214, 24
Spitler, L. R., Straatman, C. M. S., Labbé, I., et al. 2014, ApJL, 787, L36
Stefanon, M., Marchesini, D., Rudnick, G. H., Brammer, G. B., & Whitaker, K. E. 2013, ApJ, 768, 92
Straatman, C. M. S., Labbé, I., Spitler, L. R., et al. 2014, ApJL, 783, L14
Szokoly, G. P., Bergeron, J., Hasinger, G., et al. 2004, ApJS, 155, 271
Trujillo, I., Förster Schreiber, N. M., Rudnick, G., et al. 2006, ApJ, 650, 18
van der Wel, A., Bell, E. F., Häussler, B., et al. 2012, ApJS, 203, 24
van der Wel, A., Franx, M., van Dokkum, P. G., et al. 2014, ApJ, 788, 28
van Dokkum, P. G., Franx, M., Kriek, M., et al. 2008, ApJL, 677, L5
Wellons, S., Torrey, P., Ma, C.-P., et al. 2015, MNRAS, 449, 361
Wiklind, T., Dickinson, M., Ferguson, H. C., et al. 2008, ApJ, 676, 781
Williams, R. J., Quadri, R. F., Franx, M., van Dokkum, P., & Labbé, I. 2009, ApJ, 691, 1879
Xue, Y. Q., Luo, B., Brandt, W. N., et al. 2011, ApJS, 195, 10